Microscopic characterization reveals the diversity of EVs secreted by GFP-HAS3 expressing MCF7 cells

Capra, Janne

2022-08

Capra , J , Härkönen , K , Kyykallio , H , Vihinen , H , Jokitalo , E & Rilla , K 2022 , '
Microscopic characterization reveals the diversity of EVs secreted by GFP-HAS3 expressing
MCF7 cells ' , European Journal of Cell Biology , vol. 101 , no. 3 , 151235 . https://doi.org/10.1016/j.ejcb.2022.15123

http://hdl.handle.net/10138/345523
https://doi.org/10.1016/j.ejcb.2022.151235

European Journal of Cell Biology 101 (2022) 151235

Contents lists available at ScienceDirect

European Journal of Cell Biology

journal homepage: www.elsevier.com/locate/ejcb

Microscopic characterization reveals the diversity of EVs secreted by GFP-HAS3 expressing MCF7 cells

Janne Capra [a], Kai Härkönen [a], Heikki Kyykallio [a], Helena Vihinen [b], Eija Jokitalo [b], Kirsi Rilla [a,*]

[a] Institute of Biomedicine, University of Eastern Finland, Kuopio, Finland
[b] Electron Microscopy Unit, Institute of Biotechnology, University of Helsinki, Helsinki, Finland

ARTICLE INFO

Keywords:
Extracellular vesicle
Morphology
Hyaluronan synthase
Confocal microscopy
3D culture
Electron tomography

ABSTRACT

We have shown the connection of hyaluronan synthesis activity with the enhanced shedding of extracellular vesicles, but detailed morphological analysis of those hyaluronan-induced EVs is still missing. In this study we utilized a comprehensive set of high-resolution imaging techniques to characterize in high detail the size and morphology of EVs originating from stable MCF7 breast cancer cell line and transiently transfected cells expressing GFP-HAS3. To avoid possible artefacts or loss of EVs resulting from the isolation process, special attention was paid to analysis of EVs *in situ* in monolayer and in 3D cultures. The results of this study show that GFP-HAS3 expressing MCF7 cells produce morphologically diverse EVs but also demonstrates the variation in results obtained with different experimental setup, which emphasizes the importance of comparison between different methods when interpreting the observations.

1. Introduction

Extracellular vesicles (EVs) are gaining attention because of their multiple roles in cellular signaling and wide potential in biomedical applications. While the research interest toward this highly attractive research area arises, the increasing data arises new questions about EV origin, formation, and biological functions (van Niel et al., 2018). The number of described EV subgroups increases and new data on multiple shapes and budding mechanisms are continuously emerging. There is increasing evidence on big EVs, called oncosomes, secreted by cancer cells such as prostate cancer (di Vizio et al., 2009) and glioma cells (Yekula et al., 2020). Furthermore, cryo-electron microscopy has revealed a large spectrum of EVs in human seminal fluid (Höög and Lötvall, 2015), in isolates from a human mast cell line (HMC-1) (Zabeo et al., 2017) and in cerebrospinal fluid (Emelyanov et al., 2020).

Imaging methods have proven to be necessary to study the biology of EVs (Verweij et al., 2021), and especially when studying the morphology or release mechanisms of EVs, high resolution imaging is a prerequisite to obtain reliable data. Additionally, to understand the heterogeneity of EVs, it is essential to develop and utilize high resolution methods for accurate characterization of individual EVs. Super-resolution light microscopy techniques, such as PALM, dSTORM, and STED (Grapp et al., 2013; Mondal et al., 2019; Nizamudeen et al., 2018) have shown promising results on accurate characterization of individual EVs. Correlative light and electron microscopy (CLEM), which combines the labeling power of fluorescence imaging with the high resolution of electron microscopy, has been utilized for analysis of EV release mechanisms (Sung et al., 2015; Verweij et al., 2018), detection of single EVs (Arasu et al., 2017), and their binding to the target cells (Arasu et al., 2019a, 2019b).

Different plasma membrane extensions with actin core are an important source for EV formation in many different cell types (Rilla, 2021). Hyaluronan is an extracellular glycosaminoglycan that impacts EV formation from plasma membrane protrusions (Rilla et al., 2013). Overexpression of hyaluronan synthase (HAS), which is active only on the plasma membrane (Rilla et al., 2005), is known to induce formation of different plasma membrane protrusions (Kultti et al., 2006) and enhance shedding of EVs (Rilla et al., 2013). We have characterized the size distribution based on NTA analysis and molecular contents of these EVs (Arasu et al., 2019a, 2019b; Deen et al., 2016), but no detailed morphological analysis has been performed before.

In this study, we combined different techniques to characterize the

Abbreviations: BME, Basement Membrane Extract; CLEM, Correlative light and electron microscopy; GFP, Green fluorescent protein; HAS3, hyaluronan synthase 3; EV, Extracellular vesicle.

* Correspondence to: Institute of Biomedicine, University of Eastern Finland, P.O.B. 1627, FIN-70211 Kuopio, Finland.
E-mail address: kirsi.rilla@uef.fi (K. Rilla).

https://doi.org/10.1016/j.ejcb.2022.151235
Received 23 December 2021; Received in revised form 5 May 2022; Accepted 9 May 2022
Available online 11 May 2022

EVs derived from inducible hyaluronan synthase 3-(HAS3)-overexpressing human breast cancer MCF7 cells. We characterized the EV size distribution and morphology with high resolution imaging techniques such as confocal microscopy, scanning electron microscopy, correlative light and electron microscopy and 3D electron tomography. We focused especially on size distribution, morphology, and putative ways of shedding of EVs in monolayer and 3D cultures. We also compared the EV size distribution data obtained from EM image analysis with nanoparticle tracking analysis.

This work shows that HAS3 expressing MCF7 breast cancer cells produce EVs of diverse shapes and sizes (50–5000 nm). Especially EVs originating from protrusions interacting with neighboring cells were increased upon HAS3 overexpression, suggesting EV-mediated contact-dependent interactions between cells. Comparison of the size distribution of EVs secreted by these cells with SEM, 3D-TEM and NTA resulted in different results, which emphasizes the importance of combinations of different analysis methods to increase the reliability of results.

2. Materials and methods

2.1. Cell culture

The human breast adenocarcinoma MCF-7 cell line with stable, inducible expression of GFP-HAS3 has been created and characterized before in Deen et al. (2014), Siiskonen et al. (2013). The cells were cultured in minimum essential medium alpha (MEMα, EuroClone, Pavia, Italy) supplemented with 5% fetal bovine serum (FBS, HyClone, Thermo Scientific, Epsom, UK), 2 mM glutamine (EuroClone), 50 μg/ml streptomycin sulfate, and 50 U/ml penicillin (EuroClone). Cells were passaged twice a week at a 1:5 split ratio using 0.05% trypsin (w/v) 0.02% EDTA (w/v) (Biochrom AG, Berlin, Germany). For maintenance, the culture medium was supplemented with 50 μg/ml hygromycin B, but during the experiments, cells were grown without hygromycin B. To induce GFP-HAS3 overexpression, 0.5 μg/ml of doxycycline (Doxycycline hydrochloride, Sigma, St. Louise, USA) was used. For experiments for EV collection/analysis, cells were cultured in a growth medium supplemented with vesicle-free serum. The serum was purified by centrifugation at 115,000 × *g* overnight at 4 °C, and sterile filtered with a 0.2 μm filter (Sartorius, Goettingen, Germany). For transient transfections of GFP-HAS3 construct (Rilla et al., 2012), TurboFect-transfection reagent (Thermo Fisher Scientific) was used according to manufactures's instructions.

2.2. Confocal microscopy

The fluorescent images were obtained with a Zeiss Axio Observer inverted microscope (40 × NA 1.3 oil or 63 × NA 1.4 oil–objectives) and LSM700 confocal module equipped with differential interference contrast detector or LSM800 confocal module with Airyscan super-resolution technique (Carl Zeiss Microimaging GmbH, Jena, Germany). For live cell imaging, Zeiss XL-LSM S1 incubator with temperature and CO2 control was utilized. ZEN 2.3 SP1 (black) software (Carl Zeiss Microimaging GmbH) and ImageJ software (National Institute of Health, Bethesda, MD, USA) were utilized for image processing, 3D rendering and image analysis.

2.3. 3D cultures and spheroids

For MCF-7 cell 3D cultures, 50,000 cells were mixed with Cultrex Basement Membrane Extract (BME) gel (Trevigen, Gaithersburg, MD, USA). The gel was polymerized at 37 °C for 1 h and the cells were grown for 72 h. The live cultures were imaged with confocal microscopy, fixed and immunostained with CD44 antibody for size analysis or processed for electron tomography as described below.

2.4. Electron tomography

For 3D electron tomography, the spheroids of MCF7 cells grown in the gel were fixed with 2% glutaraldehyde (EM-grade, Sigma-Aldrich, Espoo, Finland) and 1.5% formaldehyde (EM-grade, Electron Microscopy Sciences, Hatfield, PA) in 0.1 M sodium cacodylate buffer pH 7.4, supplemented with 2 mM $CaCl_2$ for 2 h at RT. After washing with 0.1 M sodium cacodylate buffer the cells were post-fixed with 1% non-reduced osmium tetroxide in 0.1 M sodium cacodylate buffer for 1 h on ice. The specimens were then washed with buffer and dehydrated in ethanol series and acetone prior gradual infiltration into Epon (TAAB 812, Aldermaston, UK). After polymerization overnight at 60 °C, serial 230-nm-thick sections were cut with a 35° diamond knife (Diatome, Switzerland) on Leica EM Ultracut UC7 ultramicrotome (Leica Mikrosysteme GmbH, Austria) and collected on Pioloform-coated single slot copper grids.

Dual axis tilt series were recorded from three to four consecutive semi-thick sections using SerialEM (Mastronarde, 1997) software running on a Tecnai FEG 20 transmission electron microscope (FEI Company, part of Thermo Fisher Scientific, The Netherlands) operated at 200 kV, high tilt specimen holder (model 2020; E.A. Fischione Instruments, USA) and a 4k × 4k Ultrascan 4000 CCD camera (Gatan Inc., Pleasanton, CA). The tilt series were acquired at one-degree intervals between ± 62° at nominal magnification of 11,500 × and 10-nm gold particles placed on both grid faces served as fiducial markers for alignment. Prior alignment and reconstruction with IMOD software package, version 4.9.0 (Kremer et al., 1996) the images were binned by two providing a pixel size of 1.94 nm. Segmentation and statistical analysis were done using MIB; version 2.22 (Belevich et al., 2016) and visualization with Amira (version 5.3.2, Visage Imaging Inc./Thermo Fisher Scientific, USA). The diameter of individual EV was calculated as axis lengths from modeled tomograms of individual EVs.

2.5. Nanoparticle tracking analysis

The size distribution and number of the EVs in MCF7 culture media were analyzed with the Nanoparticle Tracking Analyzer (Malvern Instruments Ltd., Malvern, UK) with a NS300 view unit. First the conditioned culture media were filtered with 5 μm syringe filter (Sartorius, Goettingen, Germany) to remove cell debris. To collect the different EV populations, filtered media were centrifuged 10,000 × *g* for 90 min at 4 °C and the pellet was suspended to PBS (= 10,000 × *g* population). The supernatants from previous step were collected and centrifuged at 110,000 × *g* for 90 min at 4 °C, followed by suspension to PBS (= 110,000 × *g* population). To collect the whole EV population the pellets from both centrifugation steps were suspended into PBS and combined. The following settings were used for data acquisition: camera level 13, acquisition time 30 s and detection threshold 3. Data analysis was performed with the NTA v3.1 software (NanoSight, Amesbury, UK). Data for each sample was obtained from three replicates.

2.6. Western blotting

EV pellets were lysed using RIPA lysis buffer (150 mM NaCl, 50 mM Tris, 1% Nonidet P-40, 0.5% sodium deoxycholate, and 0.1% SDS) containing 10 mM NaF, and 0.5% protease inhibitor cocktail (Sigma–Aldrich, St. Louis, MO, USA). Protein content was determined using a Pierce BCA protein assay kit (Thermo Scientific, Epsom, UK). An equal amount of protein fractions was subjected to 10% SDS-PAGE and transferred to nitrocellulose membranes (Whatman, Sigma–Aldrich, St. Louis, MO, USA), blocked with 5% bovine serum albumin (BSA) in 1 × TBST (Tris-buffered saline containing 0.1% Tween 20) for 1 h at room temperature, followed by overnight incubation with anti-GFP antibody (Molecular Probes, Eugene, OR), anti-CD44 antibody (Chemicon, Temecula, CA, USA), anti-CD9 (Abcam, Cambridge, UK), anti-CD63 (Abcam) or anti-Actin (Sigma, St. Louise, USA), diluted in 1% BSA-

TBST. After 3 washes with TBST the membranes were incubated for 1 h at room temperature with the secondary antibodies (1:5000, Abcam, Cambridge, UK), diluted in 1% BSA-TBST and washed with TBST. The protein bands in the blots were visualized on a LI-COR Odyssey infrared imaging system (LI-COR Biosciences, Lincoln, NE, USA).

2.7. Scanning electron microscopy

Scanning electron microscopy of EVs was performed like previously described (Latham et al., 2013). Briefly, EV preparations resuspended in PBS were left to settle onto poly-L-lysine-coated coverslips overnight at 4 °C, washed in 0.1 M sodium cacodylate and 0.1 M sucrose (pH 7.4) and fixed in sodium cacodylate-buffered 2% (v/v) glutaraldehyde for 30 min. Samples were postfixed in 1% osmium tetroxide and 0.1 M Na-cacodylate for 1 h and dehydrated through a graded series of ethanol. After this, samples were chemically dried with hexamethyldisilazane, air-dried, coated with chrome and imaged with Zeiss Sigma HD|VP (Zeiss, Oberkochen, Germany) scanning electron microscope at 3 kV. The size distribution of EVs was analyzed using ImageJ/FIJI plugin Trainable Weka Segmentation. The plugin was manually trained until it reliably recognized vesicles from background in SEM images. Resulting images from Trainable Weka Segmentation were blurred using Gaussian Blur with a sigma value of 1.0. Subsequently, the resulting images were converted into binary images and then the segmented EV sizes were measured using Analyze Particles plugin. Results were processed using Microsoft Excel.

3. Results

3.1. Scanning electronic microscopy analysis of HAS3 expressing MCF7 cells in monolayer cultures

To characterize the effect of HAS3 expression on cell morphology, MCF7 cells with stable, inducible GFP-HAS3 expression grown in monolayer cultures were analyzed with scanning electron microscopy (Fig. 1). The induced, GFP-HAS3 expressing cells (Fig. 1B) showed a spindle-shaped morphology and higher number of protrusions as compared to uninduced cells (Fig. 1A), which is in line with our previous findings with transiently transfected cells (Kultti et al., 2006). Interestingly, also a higher number of EVs of variable size and morphology was

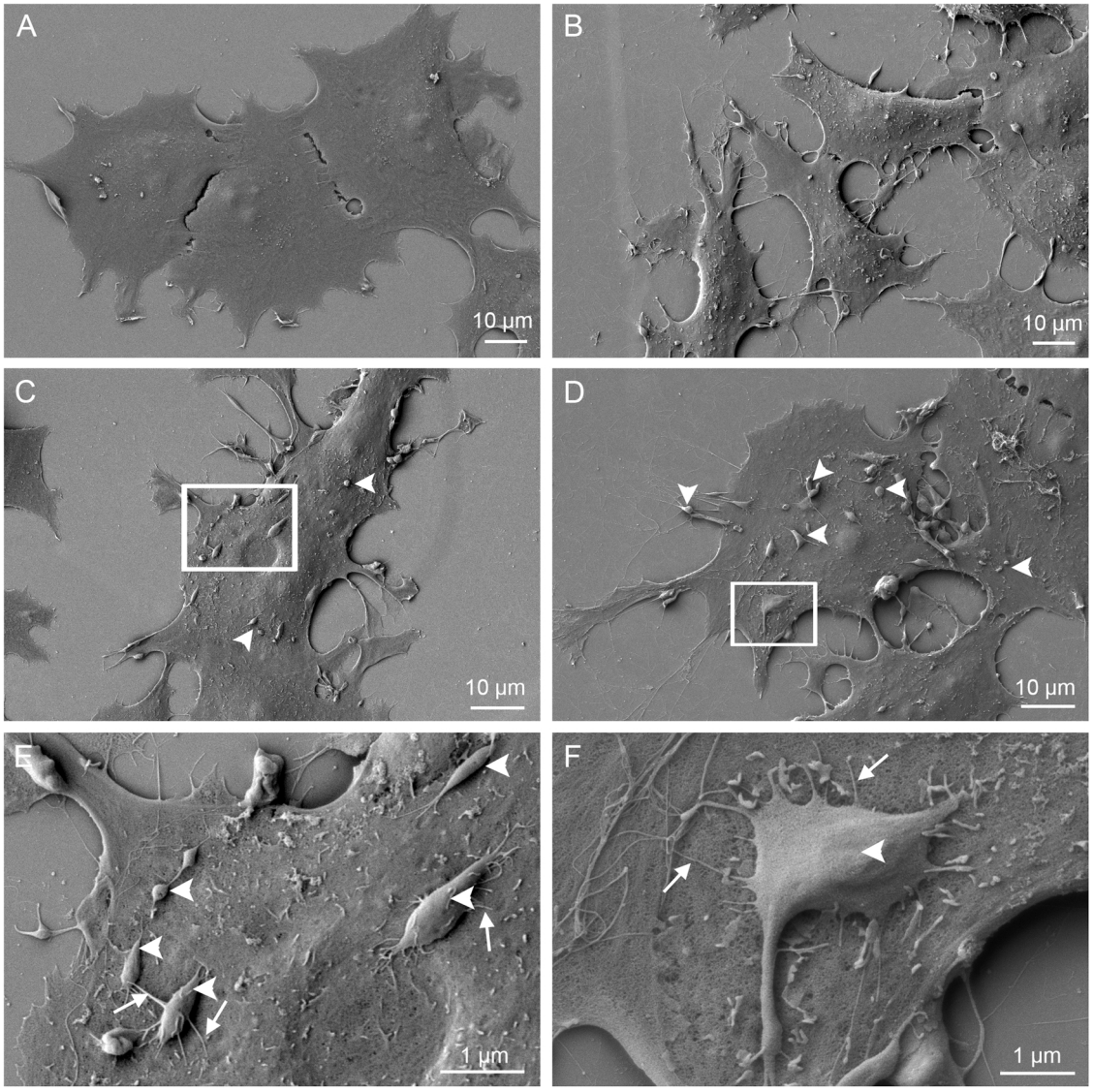

Fig. 1. Morphological characterization of MCF7 cells with stable, inducible GFP-HAS3 expression by scanning electron microscopy. Low magnification images of uninduced (A) and induced GFP-HAS3 expressing cells (B–D) in monolayer cultures. Selected areas indicated by white boxes in panels (C) and (D) show the morphology of single EVs adhered to the cell surface in higher magnification in (E) and (F), respectively. Arrows in E and F indicate the thin filopodia of large, spindle shaped EVs. Arrows point to membrane projections and arrowheads point to EVs in all panels.

adhered on the apical surface of GFP-HAS3 expressing cells (arrowheads in Fig. 1C–F) as compared to uninduced control cells. Higher magnification showed that many of the big EVs (up to 1–3 μm) adhered to the plasma membrane had small membrane tentacles (arrows in Fig. 1E and F). This suggests high variability in size and diverse morphology of EVs induced by HAS3 expression. Because no exogenous EVs were introduced to these cultures, all the detected EVs originate from HAS3 expressing cells, but it cannot be defined whether they are endogenous, originate from neighboring cells or more distant cells.

3.2. Correlative light and electron microscopy of transiently transfected MCF7 cultures reveals the juxtracrine interactions by GFP-HAS3-rich nanotubes and transfer of EVs between cells

To demonstrate in more detail the origin of these multiform cell-surface-associated EVs, a transient transfection with GFP-HAS3 plasmid for parental MCF7 cell culture was performed and analyzed by confocal and correlative light and electron microscopy (Fig. 2). This resulted in a mixture of GFP-HAS3 positive and negative cells (Fig. 2A–B), where the accumulation of GFP-HAS3 into EV membranes could be utilized as a specific marker for detection of EVs originating

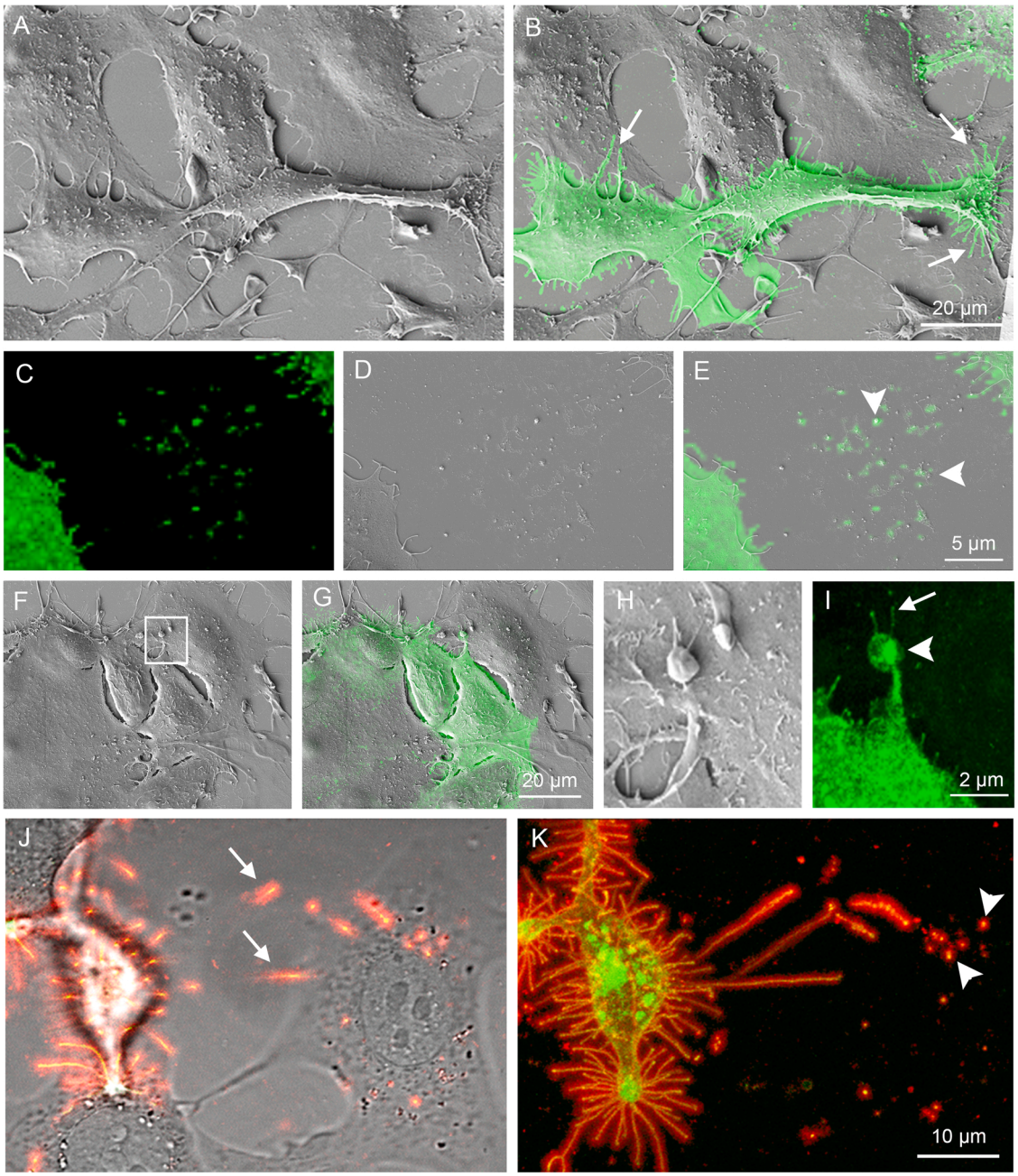

Fig. 2. Transient transfection shows that GFP-HAS3 expressing MCF7 cells are able to "seed" EVs to the substratum and to the neighboring cells. Correlative light and electron microscopy was utilized in (A–I). Panels C and I are confocal images, A, D, F and H SEM images and B, E and G overlay images. Arrows point to GFP-HAS3-positive EVs that GFP-HAS3-expressing cells "seed" to the neighboring (negative) cells or substratum. Live cell culture (J, K) shows a single GFP-HAS3 expressing cell surrounded by negative cells. Red color indicates hyaluronan detected by fluorescently labeled hyaluronan binding probe (fHABC). A combined image with differential interference contrast (DIC) and confocal optical section is shown in (J) and a maximum intensity projection created from series of optical sections of the same cell in presented in (K). Arrows in (K) indicate that GFP-HAS3- and hyaluronan-positive EVs shedding from the nanotubes adhere to the surface of the nearby cell. Arrows point to plasma membrane projections and arrowheads point to EVs in all panels.

from GFP-HAS3-expressing cells. Arrows in (B) indicate GFP-HAS3-positive nanotubes that reach and adhere to the nearby cells. A high-resolution imaging (Fig. 2C–E) revealed secreted GFP-HAS3-positive EVs attached to the bottom of the plate (arrowheads in Fig. 2E). Additionally, as suggested in Fig. 1, it was discovered that the GFP-HAS3-positive EVs that adhere to the nearby cells (arrowhead in Fig. 2I) have their own membrane projections (arrow in Fig. 2I). Additionally, live cell imaging with hyaluronan binding probe (fHABC, red) revealed that the cells have long nanotubes coated with hyaluronan, which are attached to the surface of the GFP-HAS3-negative neighboring cells (arrows in Fig. 2J). Confocal 3D projection unveiled that the nanotubes leave GFP-HAS3 -positive and hyaluronan-coated EVs to the surface of the neighboring cells, possibly as a result of detachment from the cell surface (arrowheads in Fig. 2K).

3.3. Characterization of EV size, numbers and secretion dynamics

To compare the EVs secretion by uninduced and induced MCF7 cells and to analyze the secreted EVs in more detail we isolated the EVs from MCF7 cultures with three different modifications of serial centrifugations. Increased numbers of particles upon induction of HAS3 expression was detected on NTA analysis with all three different sample types (Fig. 3A). This suggests enhanced secretion of EVs upon HAS3 expression, which is in line with our previous findings (Rilla et al., 2013; Arasu et al., 2019a, 2019b). The yield of EVs was higher in 10,000 × *g* than in 110,000 × *g*, and the best yield was received with combined samples (= total). Surprisingly, no differences in average size between the samples were detected (Fig. 3B). The kinetics of EV secretion by GFP-HAS3 expressing cells was studied by isolating the EVs at different time points during a 50-h culture period (Fig. 3C–E). There was an increase in the total numbers of particles into culture medium over time, indicating accumulation of EVs during the cell culture period (Fig. 3C). However, when the particle numbers were related to cell numbers at each time point (Fig. 3D), the number of particles per cell showed a decreasing trend (Fig. 3E), which may result from attenuated activity of EV secretion because of increased cell density and nutrient depletion and increased uptake of EVs during the culture period. The scanning electron microscopy of the EV samples from the same cells analyzed in (Fig. 3A and B) showed a high number of particles of variable size and morphology in all samples (Fig. 3F). In 10,000 × *g* isolates, occasional big EVs (500–2000 nm) were detected, but the major population consisted of smaller EVs, less than 200 nm in diameter. The 110,000 × *g*

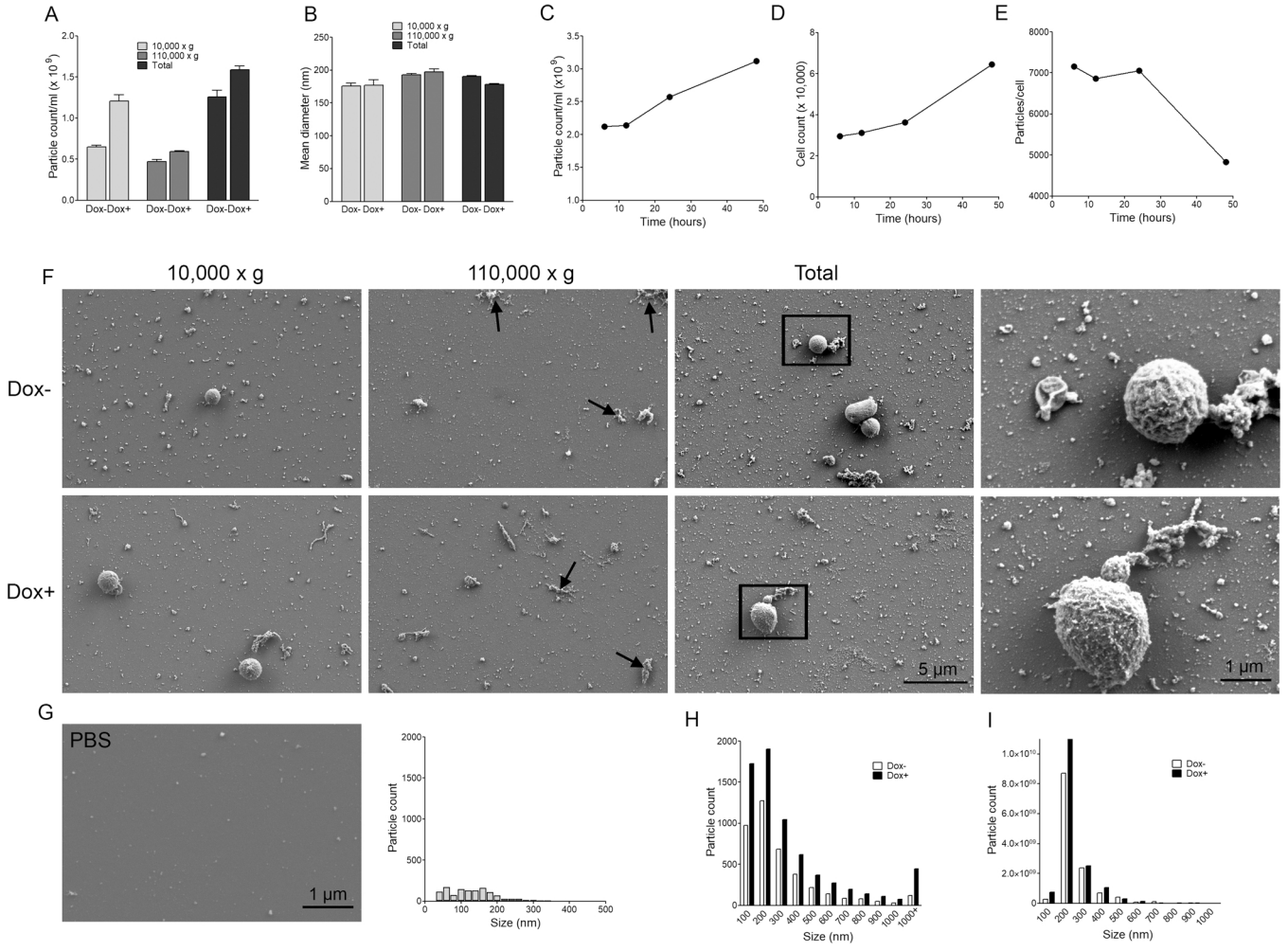

Fig. 3. Size distribution, secretion dynamics and surface morphology of EVs isolated from stable, inducible GFP-HAS3 expressing MCF7 cells. NTA analysis of EVs from culture media of uninduced (Dox-) and induced (Dox+) cells, showing size (A) and average diameter (B) from EVs isolated by 10,000 × *g*, 110,000 × *g* centrifugation and combined samples (10,000 × *g* and 110,000 × *g* = total). Error bars in A and B indicate average of two independent experiments. Particle counts (C), cell numbers (D) and particles in relation to the cell numbers (E) as a function of time in monolayer cell cultures of induced MCF7 cells, as one representative result from 3 independent repeats. Scanning electron microscopy of the EV samples isolated with 10,000 × *g*, 110,000 × *g* and combined (= total) samples (F), and PBS sample as a negative control (G). Comparison of EV size distribution in uninduced and induced MCF7 cells analyzed from SEM images (total of 5 frames from each sample) (H) and by NTA (representative data of 3 independent experiments (I).

isolates contained less large EVs, but more aggregates (on average 18% of the measured areas, arrows) as compared to 10,000 × *g* isolates (13% of the measured areas). As expected, the combined samples contained the highest number of EVs, but also big EVs and aggregates (27% of the measured areas). The high magnification images demonstrate in more detail the variable shapes and surface morphology of big EVs (Fig. 3F). The negative control containing PBS only showed some small particles, most of which were around 100 nm in diameter (Fig. 3G). A quantitative analysis from SEM images was done with combined samples (Fig. 3H). In this analysis, the smallest particles detected were 20–40 nm. The size distribution analysis shows that HAS3 expression resulted in increased EV counts in all size categories (Fig. 3H). The size distribution analyzed by NTA show similar results, but less particles in under 100 nm and over 1000 nm populations (Fig. 3I). The average diameter of analyzed

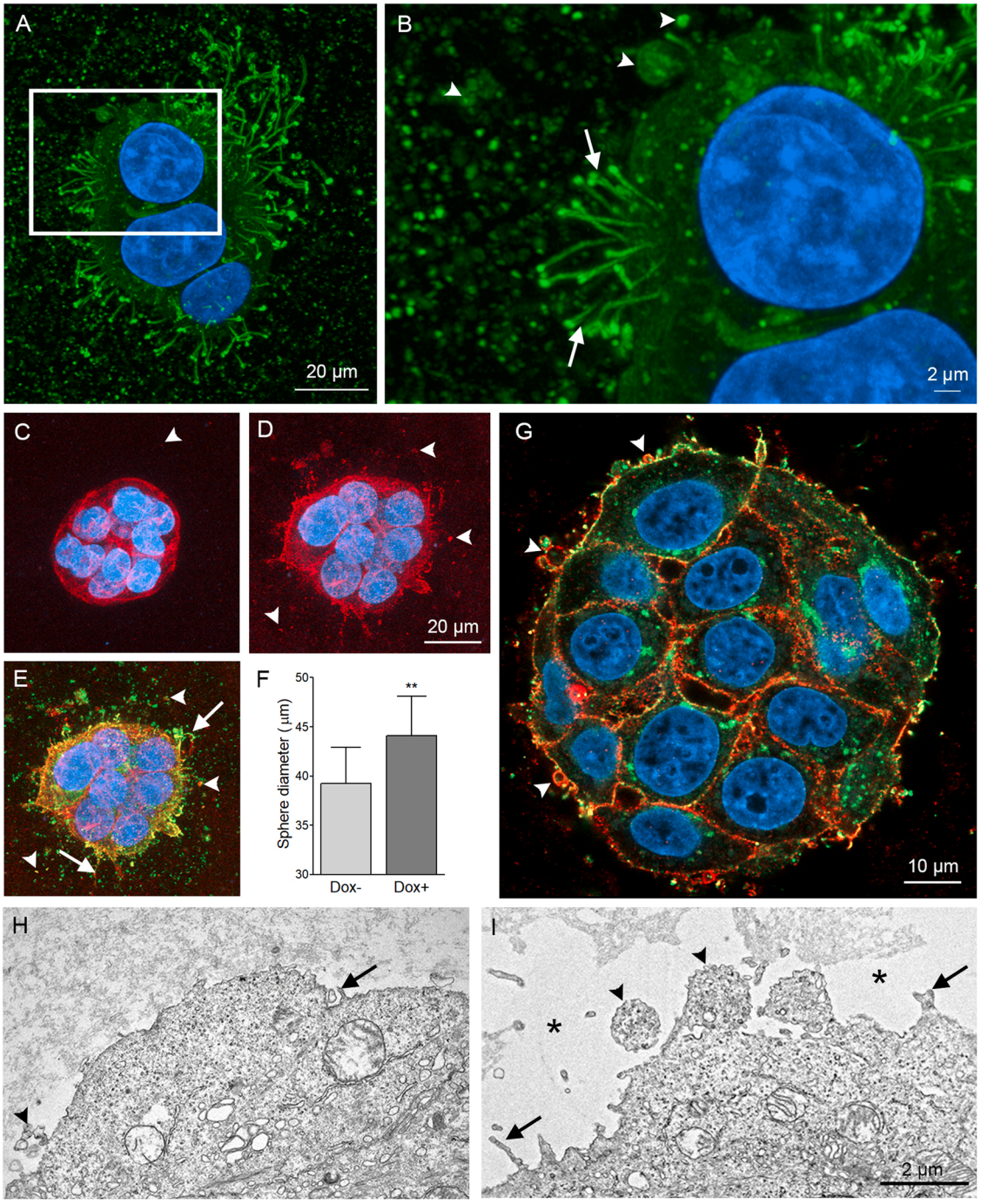

Fig. 4. A live MCF7 spheroid with stable GFP-HAS3 expression with long filopodia and high number of GFP-HAS3-positive EVs trapped in the surrounding BME matrix is shown in (A) and the area marked by white box in (A) with higher magnification in (B). Fixed and CD44-immunstained spheroids without induction (C) and with induction (D and E). Analysis of growth of uninduced (Dox-) and induced (Dox+) spheroids by measurement of spheroid diameter (n = 4 independent experiments with 68–155 spheres in each experiment) (F). An optical section imaged with superresolution (Airyscan) technique of a spheroid with GFP-HAS3 expression and CD44 immunostaining (G). Transmission electron microscopy of uninduced (H) and induced (I) spheroids from the surface facing the matrix. Asterisks in (I) show the empty areas resulting from shrinking of the sample. Arrows point to plasma membrane protrusions and arrowheads point to EVs or blebs in all panels. EVs are reliably detectable only in 3D projections (A-E), while in 2D sections of panels (G-I) EVs cannot be distinguished from membrane blebs or cross-sections of protrusions. Blue: nuclei, green: GFP-HAS3 and red: CD44 in all confocal images.

particles in uninduced and induced samples (total) was 275 and 359 nm in SEM analysis and 190 nm and 178 nm in NTA, correspondingly. Characterization of EV samples by Western Blotting demonstrated the presence of GFP-HAS3 in induced samples and several typical EV markers in both uninduced and induced EV samples (Supplementary Fig. 1).

3.4. EV secretion of GFP-HAS3 expressing MCF7 cells in 3D spheroidal cultures

To mimic more closely the *in vivo* conditions, we characterized the stable GFP-HAS3 expressing cells in a 3D environment. The cultures grown in basement membrane extract matrices were imaged with high- and superresolution 3D confocal microscopy after 72-h culture period. As expected, in live cultures a high number of filopodia and EVs were detected around the cell spheroids after induction (Fig. 4A and B). The major population of EVs detected by GFP-signal in the extracellular matrix was small, corresponding to the diameter of filopodial tips (Fig. 4B), which suggests that they originate from filopodia as previously shown (Rilla et al., 2013), but also occasional membrane blebs or large EVs were detected (arrowheads in Fig. 4B). To compare the effect of induction on the spheroid size and morphology, we fixed and immunostained the 3D cultures with antibody for hyaluronan receptor CD44 (Fig. 4C–G). The fixation resulted in collapse and disappearance of many of the filopodia, but the increased numbers of CD44-positive protrusions and particles were detected in the matrix around induced spheroids (Fig. 4D) as compared to induced ones (Fig. 4C). Many of these CD44-positive structures were colocalized with the GFP-HAS3 signal (Fig. 4E). The HAS3 expressing spheroids were significantly bigger in diameter as compared to uninduced control cells (Fig. 4F). Superresolution imaging showed in more detail the colocalization of GFP-HAS3 and CD44 signals on the membranes of protrusions, buds and EVs (arrowheads in Fig. 4G). The 3D spheroid cultures were also imaged with transmission electron microscopy. Images from the edge area of spheroids facing the surrounding matrix show a higher number of protrusions and blebs around GFP-HAS3 expressing cells (Fig. 4I) as compared to uninduced cells (Fig. 4H), which supports the findings with confocal microscopy. Additionally, empty areas were seen around the GFP-HAS3 expressing spheroids (asterisks in Fig. 4I), which indicate that high levels of hyaluronan with high water absorption capability around the cells may increase the shrinking of the matrix around HAS3 overexpressing spheroids upon dehydration process during sample preparation. On the other hand, the increased swelling pressure resulting from high concentration of hyaluronan may induce the “empty” space around cells.

3.5. Electron tomography of MCF7-derived EVs in 3D cultures in situ

To get a more detailed high-resolution analysis of spheroid-derived EVs in 3D cultures, the GFP-HAS3-induced cultures were further analyzed by electron tomography. To avoid the empty areas between cells and ECM resulting from shrinking (asterisks in Fig. 5A) and to confirm that we select EVs and not cell-associated structures for analysis, distant areas from the ECM around spheroids were selected for tomography. An example of one selected area in low magnification TEM micrograph is shown in (Fig. 5A). A detailed analysis of a cluster of EVs using electron tomography, suggests variable morphology of EVs and reveals small vesicles inside vesicles (arrows in Fig. 5B). The segmented (Fig. 5C and Supplementary movie 1) and modeled (Fig. 5D and Supplementary movie 2) tomograms of EVs illustrate in more detail the highly variable sizes and diverse shapes of EVs secreted and trapped inside the matrix. The 3D reconstruction suggests that EVs form membrane protrusions also in 3D conditions (arrow in Fig. 5D). Interestingly, a volume rendered model shows that the EVs are associated with extracellular material (arrows in Fig. 5E), and the direct contact of the extracellular material to single EVs is seen in more detail in a single

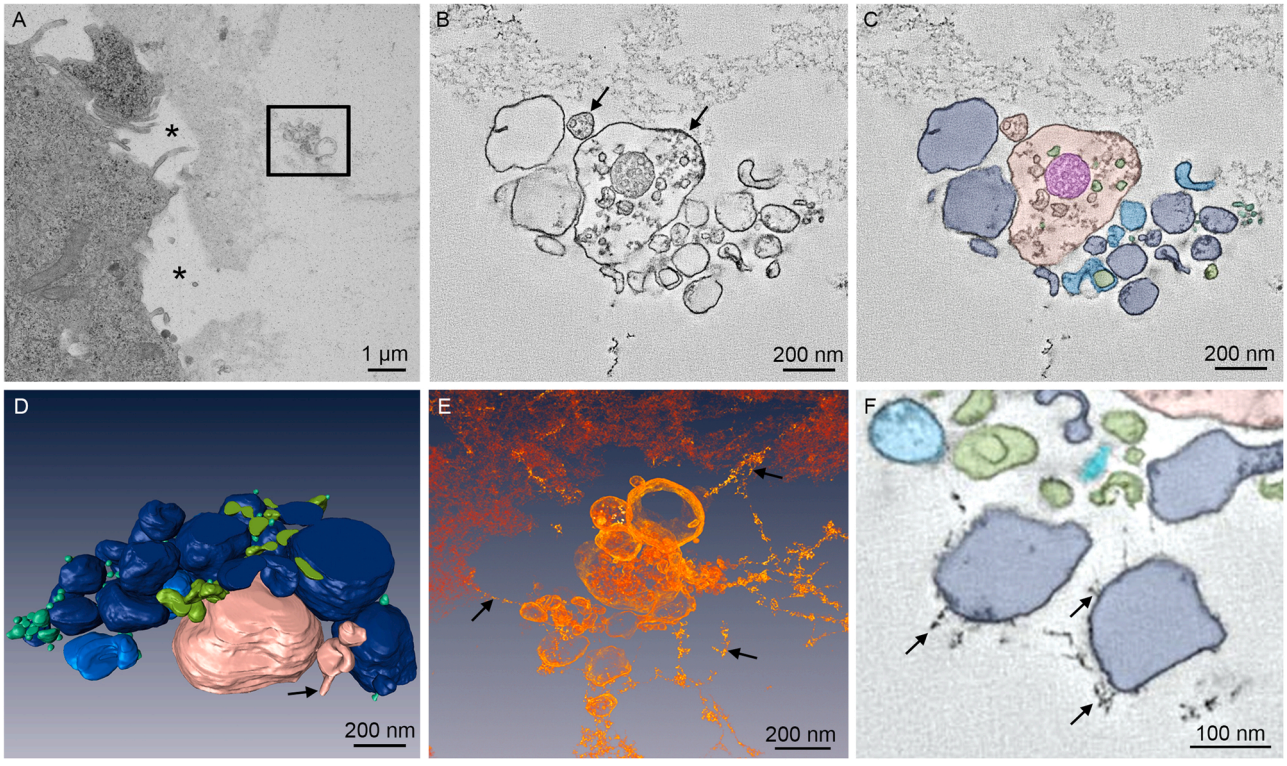

Fig. 5. Electron tomography of stable GFP-HAS3 expressing spheroids grown in BME. An overview of a 230-nm-thick section (A), an example of tomographic slice from the selected area (black box in A) (B) and the same area showing segmented vesicles (C). A 3D model generated from three serial sections showing different sizes and shapes of the vesicles (D), a volume rendered model in (E) and a tomographic slice showing in higher detail the EV interaction with ECM molecules (F). Arrows in (B) point to EVs containing smaller vesicles, arrow in (D) shows a protrusion of a vesicle and in (F) the ECM material associated with EVs.

tomographic slice (arrows in Fig. 5F).

Supplementary material related to this article can be found online at doi:10.1016/j.ejcb.2022.151235.

3.6. Comparison of different methods of analysis of EV size distribution

To summarize the data on the EV size distribution and to compare the results obtained by different methods, an analysis of the size distribution of EVs isolated from conditioned media of GFP-HAS3 expressing cells in monolayer cultures by NTA is shown in (Fig. 6A), by scanning electron microscopy in (Fig. 6B) and data analyzed from modeled tomograms of individual EVs in 3D cultures (Fig. 6C). The average diameter (mean) of EVs was 358 nm in SEM analysis, 178 nm in NTA and 110 nm in electron tomographic analysis. A higher number of small particles (under 100 nm) were detected in SEM and tomography (Fig. 6B and C) as compared to NTA (Fig. 6A). The proportion of detected EVs over 500 nm in diameter from the total population was 17.9% in SEM analysis, 1.2% in NTA and 2.7% in EM-tomography.

4. Discussion

4.1. Diversity of EVs

In this study we utilized multiple high resolution imaging techniques to characterize and analyze the size and morphology of EVs originating from HAS3 expressing MCF7 human breast cancer cells. The results revealed wide diversity in size and morphology of EVs and their interaction with the neighboring cells and the ECM. This work strengthens the current knowledge of the huge heterogenicity of EVs (Minciacchi et al., 2015; van Niel et al., 2018), which may be easily lost during isolation and purification procedures or is unrecognized in conventional analyses. On the other hand, we cannot exclude the possibility that sample preparation, *e.g.* dehydration processes in electron microscopic techniques could change the morphology of EVs.

There is increasing evidence of different protrusions as sources of EVs (Rilla, 2021), and the findings of this study support that and our previous findings of HAS3 expression as an inducer of different protrusions and EVs derived from them (Rilla et al., 2013). Additionally, we found that cells use nanotubes to sense and attach to neighboring cells, and it is possible that EVs utilize nanotubes also for enhancing of uptake of themselves or transferring from one cell to another (Franchi et al., 2020a, 2020b). These findings suggest that EVs can act as mediators of juxtracrine, contact-dependent communication between cells. Interestingly, some big EVs had their own filopodia-like protrusions, that may help EVs to adhere to target cells or facilitate their movements. It has been suggested that EVs may contain actin filaments (Höög and Lötvall, 2015), and exhibit protrusions on their surface (Zabeo et al., 2017), and large EVs that have an active cytoskeleton are capable of mobility (Johnson et al., 2017) and deformability (Lenzini et al., 2020). Furthermore, electron tomography revealed vesicles inside vesicles, which supports the previous findings from EVs in human seminal fluid (Höög and Lötvall, 2015) and from human mast cell line (HMC-1) (Zabeo et al., 2017).

4.2. The size distribution of secreted EVs

Despite of high number of large EVs that were adhered to the surface of HAS expressing cells in monolayer cultures, this was not clearly observed in NTA or SEM analysis of isolated EVs. The microscopic analysis of EVs *in situ* overemphasizes the large EVs that are attached to cell surfaces, and not secreted into culture media that is the source of isolates. Additionally, small EVs may be taken up by cells more effectively (Caponnetto et al., 2017), or are released into culture medium and not detected in cell cultures *in situ*. On the other hand, some of the largest EVs may be lost during isolation process and NTA has a limited capacity to detect big vesicles. It will be highly interesting in the future

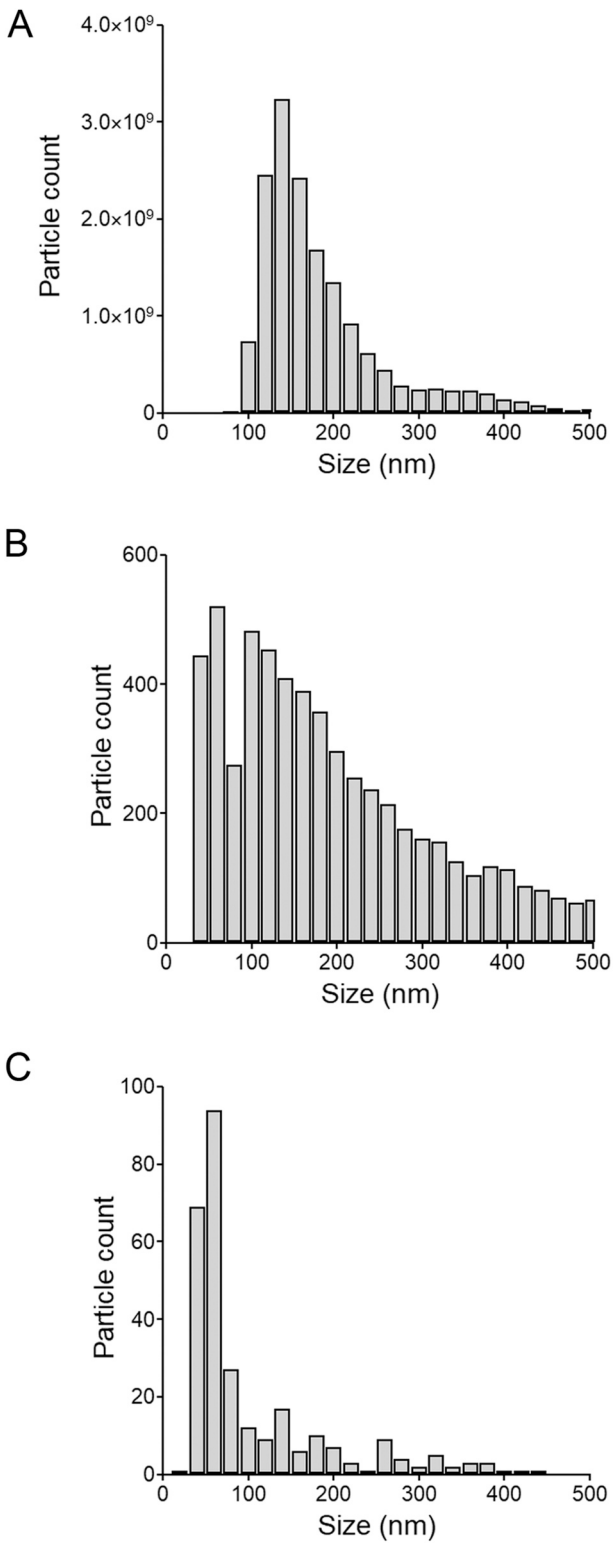

Fig. 6. Comparison of size distribution of EVs produced by HAS3 expressing MCF7 cells obtained with different methods of analysis. Nanoparticle tracking analysis (A) and scanning electron microscopic size analysis (B) of EVs isolated from monolayer cultures by differential centrifugation and electron tomographic size analysis of EVs trapped in the ECM of 3D cultures *in situ* (C). The proportion of detected EVs over 500 nm in diameter from the total population was 17.9% (1234 of 6896 particles) in SEM analysis, 1.2% (1.4×10^8 of 1.6×10^{10} particles) in NTA and 2.7% (8 of 295 particles) in EM-tomography.

to learn more about the functions of large EVs as putative messengers between cells and their fate and mobility in the ECM. Despite the proportion of these big EVs is small in total population, the cargo they carry may be significant because of their high volume. As shown in prostate cancer patient plasma (Vagner et al., 2018), large extracellular vesicles carry most of the circulating tumor DNA. Because of their bigger volume, they carry higher numbers of molecules, but they do not penetrate biological barriers or enter the target cells as effectively as smaller EVs (Caponnetto et al., 2017).

Both SEM analysis of isolates and 3D EM analysis *in situ* detected smaller MCF-7 cell derived EVs (range 20–40 nm) than standard nanoparticle tracking analysis, likely due to differences in the limits of resolution between the detection methods, but also because of the potential loss of small particles during isolation process. The minimum detectable vesicle diameter is 70–90 nm for NTA (van der Pol et al., 2014). Surprisingly, no significant differences were detected in EV preparations isolated at two different centrifugation speeds. The relatively small proportion of big EVs may explain the lack of differences between different centrifugation speed. As visualized in SEM analysis, the higher, 110,000 × *g* speed caused more aggregates that may be detected as big EVs in NTA, 10,000 × *g* sedimented also small EVs. SEM analysis of EVs in isolates gave somewhat similar results as NTA, but because of the limit of NTA to detect EVs over 1000 nm, the resulting average diameter of EVs was higher in SEM analyses as compared to NTA. The advantage of SEM analysis as analysis method or quality control for EV isolates is that it gives a comprehensive overview of the sample in good resolution, and the possible aggregates and other impurities are easily identified and can be selectively omitted from the final analysis.

It can be summarized that despite of results with similar trend, different purification methods and sample preparation techniques may be selective for certain types of EVs, and certain subpopulations of EVs may be over-represented against others. Furthermore, the sensitivity of different detection methods to different EV sizes varies (van der Pol et al., 2014). In this study the detection limit for EVs was 70–1000 nm in NTA, and a minimum of around 20 nm with no upper limit in SEM and 3D-EM analyses.

4.3. EVs in the 3D extracellular matrix

In this study, 3D cultures were utilized to analyze EVs *in situ* in an environment mimicking *in vivo* conditions and to avoid possible artefacts resulting from the isolation procedures that could selectively affect the size, morphology or recovery rate of EV. High resolution EM tomography allowed to detect and analyze a wide range of EVs of different sizes (from 20 nm to 1000 nm) and variable morphology. The detected ECM material associated with EVs supports the previous findings that EVs are integral components of the extracellular matrix (Rilla et al., 2019). In the experimental setup used in this work, it was not possible to identify the ECM molecules, but there is evidence on EV interactions with ECM proteins, such as collagens (Huleihel et al., 2016), and glycosaminoglycans (Christianson et al., 2013; Schmidt et al., 2016). It is possible that HAS3 activity and hyaluronan-coating may enhance EV mobility and deformability, which facilitates their diffusion and transport when trapped in the ECM network (Lenzini et al., 2020). Interestingly, water permeation mediated by AQP1 makes EVs more deformable (Lenzini et al., 2020). As a water binding molecule, hyaluronan may have similar effects to enhance EV deformability, and because it increases filopodia formation in cells (Rilla et al., 2013), the effect may be reflected also in secreted EVs. Additionally, hyaluronan carried on the surface of EVs modifies the extracellular niche and modulates the surface properties EVs, which may regulate the interactions of EVs with target cells.

To avoid the artefacts resulting from isolation process and to analyze intact EVs *in situ* in natural conditions, 3D-EM of 3D cultures is a promising method, but it is laborious and not suitable for high throughput analyses. Recent data suggest that also cryo-electron microscopy is a promising method to analyze structural details of EVs as shown with EVs isolated from cerebrospinal fluid (Emelyanov et al., 2020) and cell culture media (Noble et al., 2020). Future studies with these high resolution techniques are necessary to further elucidate our knowledge about the diversity of EVs in 2D and 3D conditions.

5. Conclusions

The results of this study reveal the variable size and morphology of EVs secreted by GFP-HAS3 expressing MCF7 cells in both 2D and 3D culture conditions and suggests their interaction with the extracellular matrix. The diverse morphology indicates also multiple functional properties and, in the future, may lead to discovery of previously unknown mechanisms on how EVs regulate their environment, and communicate with neighboring and distant cells and the extracellular matrix. The results widen our general understanding of the diversity of EVs and may raise new openings of EV research. The data obtained from electron tomography of EVs in 3D cultures indicates the urgent need for novel 3D cultures for even more detailed analysis of EVs in their natural environment and for novel methods for an easy isolation of EVs originating from cells cultured in 3D conditions.

Acknowledgements

Eija Rahunen, Virpi Miettinen, Silja Pyysalo, Taija Hukkanen and Mervi Lindman (EM-Unit, University of Helsinki) are acknowledged for their expert technical assistance. This project has been funded by the Academy of Finland GeneCellNano Flagship (Grant #337120), Jane and Aatos Erkko Foundation, Mizutani Foundation, Japan Paavo Koistinen Foundation and Northern Savo Cancer Foundation. This research has been supported by the EATRIS, the European Infrastructure for Translational Medicine. We are thankful for the opportunity to use the facilities of the SIB Labs and UEF Cell and Tissue Imaging Unit, Biocenter Kuopio and Biocenter Finland.

Appendix A. Supporting information

Supplementary data associated with this article can be found in the online version at doi:10.1016/j.ejcb.2022.151235.

References

Arasu, U.T., Härkönen, K., Koistinen, A., Rilla, K., 2019a. Correlative light and electron microscopy is a powerful tool to study interactions of extracellular vesicles with recipient cells. Exp. Cell Res. 376, 149–158. https://doi.org/10.1016/j.yexcr.2019.02.004.

Arasu, U.T., Kärnä, R., Härkönen, K., Oikari, S., Koistinen, A., Kröger, H., Qu, C., Lammi, M.J., Rilla, K., 2017. Human mesenchymal stem cells secrete hyaluronan-coated extracellular vesicles. Matrix Biol. 64, 54–68. https://doi.org/10.1016/j.matbio.2017.05.001.

Arasu, U.T., Deen, A.J., Pasonen-Seppänen, S., Heikkinen, S., Lalowski, M., Kärnä, R., Härkönen, K., Mäkinen, P., Lázaro-Ibáñez, E., Siljander, P.R.M., Oikari, S., Levonen, A.L., Rilla, K., 2019b. HAS3-induced extracellular vesicles from melanoma cells stimulate IHH mediated c-Myc upregulation via the hedgehog signaling pathway in target cells. Cell. Mol. Life Sci. https://doi.org/10.1007/s00018-019-03399-5.

Belevich, I., Joensuu, M., Kumar, D., Vihinen, H., Jokitalo, E., 2016. Microscopy image browser: a platform for segmentation and analysis of multidimensional datasets. PLoS Biol. 14, e1002340 https://doi.org/10.1371/journal.pbio.1002340.

Caponnetto, F., Manini, I., Skrap, M., Palmai-Pallag, T., di Loreto, C., Beltrami, A.P., Cesselli, D., Ferrari, E., 2017. Size-dependent cellular uptake of exosomes. Nanomed.: Nanotechnol. Biol. Med. 13, 1011–1020. https://doi.org/10.1016/j.nano.2016.12.009.

Christianson, H.C., Svensson, K.J., van Kuppevelt, T.H., Li, J.-P., Belting, M., 2013. Cancer cell exosomes depend on cell-surface heparan sulfate proteoglycans for their internalization and functional activity. Proc. Natl. Acad. Sci. USA 110, 17380–17385. https://doi.org/10.1073/pnas.1304266110.

Deen, A.J., Arasu, U.T., Pasonen-Seppänen, S., Hassinen, A., Takabe, P., Wojciechowski, S., Kärnä, R., Rilla, K., Kellokumpu, S., Tammi, R., Tammi, M., Oikari, S., 2016. UDP-sugar substrates of HAS3 regulate its O-GlcNAcylation, intracellular traffic, extracellular shedding and correlate with melanoma progression. Cell. Mol. Life Sci. 73, 3183–3204. https://doi.org/10.1007/s00018-016-2158-5.

Deen, A.J., Rilla, K., Oikari, S., Kärna, R., Bart, G., Häyrinen, J., Bathina, A.R., Ropponen, A., Makkonen, K., Tammi, R.H., Tammi, M.I., 2014. Rab10-mediated endocytosis of the hyaluronan synthase HAS3 regulates hyaluronan synthesis and cell adhesion to collagen. J. Biol. Chem. 289. https://doi.org/10.1074/jbc.M114.552133.

di Vizio, D., Kim, J., Hager, M.H., Morello, M., Yang, W., Lafargue, C.J., True, L.D., Rubin, M.A., Adam, R.M., Beroukhim, R., Demichelis, F., Freeman, M.R., 2009. Oncosome formation in prostate cancer: association with a region of frequent chromosomal deletion in metastatic disease. Cancer Res. 69, 5601–5609. https://doi.org/10.1158/0008-5472.CAN-08-3860.

Emelyanov, A., Shtam, T., Kamyshinsky, R., Garaeva, L., Verlov, N., Miliukhina, I., Kudrevatykh, A., Gavrilov, G., Zabrodskaya, Y., Pchelina, S., Konevega, A., 2020. Cryo-electron microscopy of extracellular vesicles from cerebrospinal fluid. PLoS One 15. https://doi.org/10.1371/JOURNAL.PONE.0227949.

Franchi, M., Piperigkou, Z., Karamanos, K.A., Franchi, L., Masola, V., 2020a. Extracellular matrix-mediated breast cancer cells morphological alterations, invasiveness, and microvesicles/exosomes release. Cells 9. https://doi.org/10.3390/cells9092031.

Franchi, M., Piperigkou, Z., Riti, E., Masola, V., Onisto, M., Karamanos, N.K., 2020b. Long filopodia and tunneling nanotubes define new phenotypes of breast cancer cells in 3D cultures. Matrix Biol. Plus 6–7, 100026. https://doi.org/10.1016/j.mbplus.2020.100026.

Grapp, M., Wrede, A., Schweizer, M., Hüwel, S., Galla, H.J., Snaidero, N., Simons, M., Bückers, J., Low, P.S., Urlaub, H., Gärtner, J., Steinfeld, R., 2013. Choroid plexus transcytosis and exosome shuttling deliver folate into brain parenchyma. Nat. Commun. 4 https://doi.org/10.1038/ncomms3123.

Höög, J.L., Lötvall, J., 2015. Diversity of extracellular vesicles in human ejaculates revealed by cryo-electron microscopy. J. Extracell. Vesicles 4, 28680. https://doi.org/10.3402/jev.v4.28680.

Huleihel, L., Hussey, G.S., Naranjo, J.D., Zhang, L., Dziki, J.L., Turner, N.J., Stolz, D.B., Badylak, S.F., 2016. Matrix-bound nanovesicles within ECM bioscaffolds. Sci. Adv. 2, e1600502 https://doi.org/10.1126/sciadv.1600502.

Johnson, S.M., Dempsey, C., Parker, C., Mironov, A., Bradley, H., Saha, V., 2017. Acute lymphoblastic leukaemia cells produce large extracellular vesicles containing organelles and an active cytoskeleton. J. Extracell. Vesicles 6, 1294339. https://doi.org/10.1080/20013078.2017.1294339.

Kremer, J.R., Mastronarde, D.N., McIntosh, J.R., 1996. Computer visualization of three-dimensional image data using IMOD. J. Struct. Biol. 116, 71–76. https://doi.org/10.1006/jsbi.1996.0013.

Kultti, A., Rilla, K., Tiihonen, R., Spicer, A.P., Tammi, R.H., Tammi, M.I., 2006. Hyaluronan synthesis induces microvillus-like cell surface protrusions. J. Biol. Chem. 281, 15821–15828. https://doi.org/10.1074/jbc.M512840200.

Latham, S.L., Chaponnier, C., Dugina, V., Couraud, P.-O., Grau, G.E.R., Combes, V., 2013. Cooperation between β- and γ-cytoplasmic actins in the mechanical regulation of endothelial microparticle formation. FASEB J.: Off. Publ. Fed. Am. Soc. Exp. Biol. 27, 672–683. https://doi.org/10.1096/fj.12-216531.

Lenzini, S., Bargi, R., Chung, G., Shin, J.W., 2020. Matrix mechanics and water permeation regulate extracellular vesicle transport. Nat. Nanotechnol. 15, 217–223. https://doi.org/10.1038/S41565-020-0636-2.

Mastronarde, D.N., 1997. Dual-axis tomography: an approach with alignment methods that preserve resolution. J. Struct. Biol. 120, 343–352. https://doi.org/10.1006/jsbi.1997.3919.

Minciacchi, V.R., Freeman, M.R., di Vizio, D., 2015. Extracellular vesicles in cancer: exosomes, microvesicles and the emerging role of large oncosomes. Semin. Cell Dev. Biol. 40, 41–51. https://doi.org/10.1016/j.semcdb.2015.02.010.

Mondal, A., Ashiq, K.A., Phulpagar, P., Singh, D.K., Shiras, A., 2019. Effective visualization and easy tracking of extracellular vesicles in glioma cells. Biol. Proced. Online 21. https://doi.org/10.1186/s12575-019-0092-2.

Nizamudeen, Z., Markus, R., Lodge, R., Parmenter, C., Platt, M., Chakrabarti, L., Sottile, V., 2018. Rapid and accurate analysis of stem cell-derived extracellular vesicles with super resolution microscopy and live imaging. Biochim. Biophys. Acta - Mol. Cell Res. 1865, 1891–1900. https://doi.org/10.1016/j.bbamcr.2018.09.008.

Noble, J.M., Roberts, L.D.M., Vidavsky, N., Chiou, A.E., Fischbach, C., Paszek, M.J., Estroff, L.A., Kourkoutis, L.F., 2020. Direct comparison of optical and electron microscopy methods for structural characterization of extracellular vesicles. J. Struct. Biol. 210 https://doi.org/10.1016/j.jsb.2020.107474.

Rilla, K., 2021. Diverse plasma membrane protrusions act as platforms for extracellular vesicle shedding. J. Extracell. Vesicles 10, e12148. https://doi.org/10.1002/jev2.12148.

Rilla, K., Mustonen, A.M., Arasu, U.T., Härkönen, K., Matilainen, J., Nieminen, P., 2019. Extracellular vesicles are integral and functional components of the extracellular matrix. Matrix Biol. 75–76, 201–219. https://doi.org/10.1016/j.matbio.2017.10.003.

Rilla, K., Pasonen-Seppänen, S., Deen, A.J., Koistinen, V.V.T., Wojciechowski, S., Oikari, S., Kärnä, R., Bart, G., Törrönen, K., Tammi, R.H., Tammi, M.I., 2013. Hyaluronan production enhances shedding of plasma membrane-derived microvesicles. Exp. Cell Res. 319, 2006–2018. https://doi.org/10.1016/j.yexcr.2013.05.021.

Rilla, K., Pasonen-Seppänen, S., Kärnä, R., Karjalainen, H.M., Törrönen, K., Koistinen, V., Tammi, M.I., Tammi, R.H., Teräväinen, T., Manninen, A., 2012. HAS3-induced accumulation of hyaluronan in 3D MDCK cultures results in mitotic spindle misorientation and disturbed organization of epithelium. Histochem. Cell Biol. 137 https://doi.org/10.1007/s00418-011-0896-x.

Rilla, K., Siiskonen, H., Spicer, A.P., Hyttinen, J.M.T., Tammi, M.I., Tammi, R.H., 2005. Plasma membrane residence of hyaluronan synthase is coupled to its enzymatic activity. J. Biol. Chem. 280, 31890–31897. https://doi.org/10.1074/jbc.M504736200.

Schmidt, J.R., Kliemt, S., Preissler, C., Moeller, S., von Bergen, M., Hempel, U., Kalkhof, S., 2016. Osteoblast-released matrix vesicles, regulation of activity and composition by sulfated and non-sulfated glycosaminoglycans. Mol. Cell. Proteom. 15, 558–572. https://doi.org/10.1074/mcp.M115.049718.

Siiskonen, H., Rilla, K., Kärnä, R., Bart, G., Jing, W., Haller, M.F., Deangelis, P.L., Tammi, R.H., Tammi, M.I., 2013. Hyaluronan in cytosol-microinjection-based probing of its existence and suggested functions. Glycobiology 23. https://doi.org/10.1093/glycob/cws149.

Sung, B.H., Ketova, T., Hoshino, D., Zijlstra, A., Weaver, A.M., 2015. Directional cell movement through tissues is controlled by exosome secretion. Nat. Commun. 6, 7164. https://doi.org/10.1038/ncomms8164.

Vagner, T., Spinelli, C., Minciacchi, V.R., Balaj, L., Zandian, M., Conley, A., Zijlstra, A., Freeman, M.R., Demichelis, F., De, S., Posadas, E.M., Tanaka, H., di Vizio, D., 2018. Large extracellular vesicles carry most of the tumour DNA circulating in prostate cancer patient plasma. J. Extracell. Vesicles 7. https://doi.org/10.1080/20013078.2018.1505403.

van der Pol, E., Coumans, F.A.W., Grootemaat, A.E., Gardiner, C., Sargent, I.L., Harrison, P., Sturk, A., van Leeuwen, T.G., Nieuwland, R., 2014. Particle size distribution of exosomes and microvesicles determined by transmission electron microscopy, flow cytometry, nanoparticle tracking analysis, and resistive pulse sensing. J. Thromb. Haemostasis 12, 1182–1192. https://doi.org/10.1111/jth.12602.

van Niel, G., D'Angelo, G., Raposo, G., 2018. Shedding light on the cell biology of extracellular vesicles. Nat. Rev. Mol. Cell Biol. https://doi.org/10.1038/nrm.2017.125.

Verweij, F.J., Bebelman, M.P., Jimenez, C.R., Garcia-Vallejo, J.J., Janssen, H., Neefjes, J., Knol, J.C., de Goeij-de Haas, R., Piersma, S.R., Baglio, S.R., Verhage, M., Middeldorp, J.M., Zomer, A., van Rheenen, J., Coppolino, M.G., Hurbain, I., Raposo, G., Smit, M.J., Toonen, R.F.G., van Niel, G., Pegtel, D.M., 2018. Quantifying exosome secretion from single cells reveals a modulatory role for GPCR signaling. J. Cell Biol. 217, 1129–1142. https://doi.org/10.1083/jcb.201703206.

Verweij, F.J., Balaj, L., Boulanger, C.M., Carter, D.R.F., Compeer, E.B., D'Angelo, G., el Andaloussi, S., Goetz, J.G., Gross, J.C., Hyenne, V., Krämer-Albers, E.M., Lai, C.P., Loyer, X., Marki, A., Momma, S., Nolte-'t Hoen, E.N.M., Pegtel, D.M., Peinado, H., Raposo, G., Rilla, K., Tahara, H., Théry, C., van Royen, M.E., Vandenbroucke, R.E., Wehman, A.M., Witwer, K., Wu, Z., Wubbolts, R., van Niel, G., 2021. The power of imaging to understand extracellular vesicle biology in vivo. Nat. Methods 18, 1013–1026. https://doi.org/10.1038/s41592-021-01206-3.

Yekula, A., Minciacchi, V.R., Morello, M., Shao, H., Park, Y., Zhang, X., Muralidharan, K., Freeman, M.R., Weissleder, R., Lee, H., Carter, B., Breakefield, X.O., di Vizio, D., Balaj, L., 2020. Large and small extracellular vesicles released by glioma cells in vitro and in vivo. J. Extracell. Vesicles 9, 1689784. https://doi.org/10.1080/20013078.2019.1689784.

Zabeo, D., Cvjetkovic, A., Lässer, C., Schorb, M., Lötvall, J., Höög, J.L., 2017. Exosomes purified from a single cell type have diverse morphology. J. Extracell. Vesicles 6, 1329476. https://doi.org/10.1080/20013078.2017.1329476.